



HAL
open science

Micromechanical behaviour of a two-phase Ti alloy studied using grazing incidence diffraction and a self-consistent model

Yuchen Zhao, Sebastian Wroński, Andrzej Baczmanski, Léa Le Joncour, Marianna Marcizko, T. Tokarski, Mathias Wrobel, Manuel François, Benoît Panicaud

► To cite this version:

Yuchen Zhao, Sebastian Wroński, Andrzej Baczmanski, Léa Le Joncour, Marianna Marcizko, et al.. Micromechanical behaviour of a two-phase Ti alloy studied using grazing incidence diffraction and a self-consistent model. *Acta Materialia*, 2017, 136, pp.402-414. 10.1016/j.actamat.2017.06.022 . hal-02279313

HAL Id: hal-02279313

<https://utt.hal.science/hal-02279313>

Submitted on 28 Aug 2023

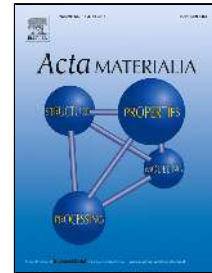
HAL is a multi-disciplinary open access archive for the deposit and dissemination of scientific research documents, whether they are published or not. The documents may come from teaching and research institutions in France or abroad, or from public or private research centers.

L'archive ouverte pluridisciplinaire **HAL**, est destinée au dépôt et à la diffusion de documents scientifiques de niveau recherche, publiés ou non, émanant des établissements d'enseignement et de recherche français ou étrangers, des laboratoires publics ou privés.

Accepted Manuscript

Micromechanical behaviour of a two-phase Ti alloy studied using grazing incidence diffraction and a self-consistent model

Y. Zhao, S. Wroński, A. Baczmański, L. Le Joncour, M. Marciszko, T. Tokarski, M. Wróbel, M. François, B. Panicaud



PII: S1359-6454(17)30497-4
DOI: 10.1016/j.actamat.2017.06.022
Reference: AM 13857
To appear in: *Acta Materialia*
Received Date: 21 March 2017
Revised Date: 09 June 2017
Accepted Date: 09 June 2017

Please cite this article as: Y. Zhao, S. Wroński, A. Baczmański, L. Le Joncour, M. Marciszko, T. Tokarski, M. Wróbel, M. François, B. Panicaud, Micromechanical behaviour of a two-phase Ti alloy studied using grazing incidence diffraction and a self-consistent model, *Acta Materialia* (2017), doi: 10.1016/j.actamat.2017.06.022

This is a PDF file of an unedited manuscript that has been accepted for publication. As a service to our customers we are providing this early version of the manuscript. The manuscript will undergo copyediting, typesetting, and review of the resulting proof before it is published in its final form. Please note that during the production process errors may be discovered which could affect the content, and all legal disclaimers that apply to the journal pertain.

Micromechanical behaviour of a two-phase Ti alloy studied using grazing incidence diffraction and a self-consistent model

Y. Zhao¹, S. Wroński², A. Baczmański^{2*}, L. Le Joncour¹, M. Marciszko³,
T. Tokarski³, M. Wróbel⁴, M. François¹ and B. Panicaud¹

¹ICD-LASMIS, Université de Technologie de Troyes (UTT), UMR CNRS 6281, 12
rue Marie Curie, CS 42060, 10004 Troyes, France

²AGH- University of Science and Technology, Faculty of Physics and Applied
Computer Science, al. Mickiewicza 30, 30-059 Krakow, Poland

³AGH- University of Science and Technology, Academic Centre for Materials and
Nanotechnology, al. Mickiewicza 30, 30-059 Krakow, Poland

⁴AGH- University of Science and Technology, Faculty of Metals Engineering
and Industrial Computer Science, al. Mickiewicza 30, 30-059 Krakow, Poland

Keywords: elasto-plastic deformation, polycrystalline material, self-consistent model,
grazing incidence angle, X-ray diffraction

Abstract

The mechanical behaviour of each phase in two-phase titanium Ti-18 was studied at room temperature under a low strain rate tensile test until fracture. Due to its selectivity, the X-ray diffraction method was applied for *in-situ* tensile test to analyse the behaviour of each phase in the direction perpendicular to the loading force. In addition, the biaxial stress states of the initial sample, as well as those of the sample during the tensile test, were determined using multi-reflection grazing incidence X-ray diffraction (MGIXD). The experimental data were compared with the prediction of an elasto-plastic self-consistent model in order to study slips on crystallographic planes and mechanical effects occurring during plastic deformation.

* Corresponding author Andrzej.Baczmański@fis.agh.edu.pl

1. Introduction

Due to a high strength-density ratio, as well as excellent chemical and mechanical resistance, titanium is widely used in industrial applications. At low temperatures, titanium crystallises in a hexagonal close-packed (hcp) structure called α -phase. Above its transus temperature ($882 \pm 2^\circ\text{C}$), it is transformed into a stable body-centered cubic (bcc) structure referred to as β -phase.

The elasto-plastic deformation of titanium alloys is determined by the activation of slips and the twinning process occurring in each phase of the material, as well as intergranular and interphase interactions in polycrystalline aggregates. In the case of bcc crystals (β -phase) the pencil glide, i.e. the slip systems: $\{011\}\langle 11\bar{1}\rangle$, $\{112\}\langle 11\bar{1}\rangle$ and $\{123\}\langle 11\bar{1}\rangle$ are active during plastic deformation [1]. A greater number of glide systems occur in the hexagonal hcp lattice than in the cubic structure. The prismatic slip system P $\langle a \rangle$: $\{\bar{1}100\}\langle 11\bar{2}0 \rangle$ is the main active system, while the basal B $\langle a \rangle$: $\{0002\}\langle 11\bar{2}0 \rangle$, pyramidal $\Pi_1 \langle c+a \rangle$: $\{\bar{1}011\}\langle 11\bar{2}3 \rangle$ and pyramidal $\Pi_1 \langle a \rangle$: $\{\bar{1}101\}\langle 11\bar{2}0 \rangle$ systems are considered secondary in the α -phase of Ti [1–7]. Mechanical twinning, the other mechanism of the plastic deformation can occur in the α -phase, however in two-phase titanium alloys this phenomenon is suppressed by oxygen and aluminium components and in this case the twins can appear only after some deformation by slip (e.g. in Ti-6Al-4V for deformation above 4% [1,8])

As a selective and non-destructive method, the diffraction method applied here for *in-situ* tensile test is particularly useful in analysing the evolution of phase behaviour during elastic and elasto-plastic deformation. This experimental technique enables determination of the average elastic strain for grain subsets situated inside the gauge volume defined by diffraction condition. The measurements are carried out using selected hkl reflections for different directions of the scattering vector with respect to the sample during tensile/compression tests or cycling loading [5,6,9–17]. In the case of multiphase polycrystalline materials, the

measurement of separate diffraction peaks enables independent investigations of the behaviour of each phase [10–17].

The results of experiments are usually then compared with the predictions of micromechanical models in order to interpret the observed evolution of lattice strains during deformation [5,6,9–14]. Heretofore, many studies have concerned the identification of initial critical resolved shear stress (CRSS) and parameters of work hardening models characterising crystallographic slips, as well as analysis of the twinning phenomenon occurring in single- or two-phase materials. The measurements are generally done using the transmission method during an *in-situ* tensile/compressive test; the lattice strains are determined in the direction of the applied load and in the transverse direction. To accomplish this, radiation with a low rate of absorption in the studied material must be used; therefore the most suitable techniques for such experiments are the neutron [5,6,9,10,11,14–15] and high-energy synchrotron diffraction methods [12–13,16,17].

Two-phase titanium alloys were investigated using the neutron [14,15], synchrotron [16,17] as well as classical diffraction methods [18]. Using diffraction during *in-situ* tensile test the values of CRSS in both phases were determined by comparing self-consistent model with measured lattice strains [14–17]. Moreover, a very good agreement of measured and model lattice strains characterising anisotropic intergranular stresses within α -phase was found in Ti–6Al–4V alloy [15,16]. In the above cited works [14–17] the single crystal elastic constants (SECs) of both phases were determined in different two-phase titanium alloys. The measurements performed for different alloys showed similar values of SECs for α -phase [19], while in the case of β -phase elastic properties of crystal depend strongly on alloying components as well as on the thermal treatment. It should be also stated that due to low coherent neutron scattering of titanium, and/or a small content of a given phase, the lattice strains were measured only for one reflection in β -phase [15–16] or not measured determined

in α -phase [14]. Therefore in these works the information about one of the studied phases was limited. The most representative data concerning elasticity of β -phase (3 reflections) as well as α -phase (7 reflections) were obtained using high-energy synchrotron diffraction for *in-situ* tensile test performed for aged and forged Ti–10V–2Fe–3Al alloy [17]. It was found that the SEC of β -phase are very different after two thermal treatments, while α -phase do not change significantly. Also, the standard Cu K α X-ray radiation was used to determine SEC of β -phase from lattice strains for Ti-17 alloy subjected to applied load [18]. However, in this work the properties of α -phase as well as plastic behaviour of the sample were not studied.

Contrary to previous experiments conducted with neutron or high-energy synchrotron radiation, the present paper proposes an original diffraction method for study of elasto-plastic behaviour of two-phase Ti alloy, performed in reflection mode on a laboratory diffractometer. Due to the excellent coherent scattering of X-rays by titanium and a significant content of both phases, sufficient diffraction intensity was registered for large diffraction patterns containing reflections from both β - and α -phases, even in the case of strongly textured sample. Thanks to the use of the multi-reflection grazing incidence X-ray diffraction (MGIXD) technique [20-28], not only the lattice strains but also the mean stresses in each phase, i.e. the stress partitioning between phases, were determined experimentally. In the present work the SEC given in Table 1 were used in model prediction and to calculate stresses in both phases. In the case of β - phase different sets of elastic constants found in literature were verified.

The measured lattice strains as well as the mean phase stresses were also successfully compared with the predictions of an elasto-plastic self-consistent (EPSC) model [29,11] based on Eshelby's inclusion scheme.

2. Material characterisation and experimental techniques

The experiments were carried out on the newly developed high-strength titanium alloy TIMETAL 18 (called Ti-18) produced by the TIMET company (Exton, Pennsylvania, USA)

and received as a quarter of an ingot, with a diameter of 250 mm. This ingot was prepared by means of vacuum arc remelting, then forged and rolled below the beta transformation temperature equal to 1136 K. Subsequently, the material was processed by means of solution heat treatment at a subtransus temperature (1089K) for 2 hours, then air-cooled. Finally it was treated by precipitation hardening at 894K for 8 hours (aging) and then air-cooled. The chemical composition of the studied alloy is shown in Table 2.

The characteristic bi-modal microstructure of Ti-18 alloy consists of uniformly distributed equiaxed primary α_p -phase grains and lamellar secondary α_s -phase inclusions embedded in β - phase matrix (cf. Fig.1). The α_p grains are transformed from β -titanium due to sub-transus solution treatment treatment, while the lamellar α_s inclusions appear during the precipitation hardening process [30]. The volume fraction of α -phase estimated from SEM images is equal to $45\% \pm 5\%$.

To determine microstructures of initial and fractured (deformed) samples the Transmission Kikuchi Diffraction (TKD) method [31,32] was used. TKD methodology offers much better spatial resolution in comparison with standard EBSD technique, therefore the orientation maps acquired with a step of 20 nm allowed us to determine reasonable images for α_s lamellas (acquisition parameters were set according to [32]). The results of TKD analysis, in the form of raw data without any map cleaning procedures, are shown in Fig. 2. As expected for small sample strain E_{11} of about 4.5%, no significant differences between the initial and deformed samples are observed and no twins were found in both phases of the studied Ti-18 alloy. The inverse pole figures (IPF) maps show homogenous lattice orientation in β -phase as well as within α_p precipitates. Analysis of the image quality (IQ) maps shows that the worse quality of Kikuchi patterns (dark shade of gray) were obtained for α_s precipitates possibly due their small size (both α and β phases are present in the gauge volume studied by TKD) or possibly due to higher density of defects.

A PANalytical X'Pert MPD diffractometer using not filtered Cu radiation ($\lambda_{K\alpha_1} = 1.54056$ Å and $\lambda_{K\alpha_2} = 1.54439$ Å) was employed to perform measurements of interplanar spacings (lattice strains) and to characterise the crystallographic texture. In the case of strain measurements, a Göbel mirror (divergence of beam 0.8°) was used to collimate the incident beam, while a parallel collimator with Soller slits (divergence 0.18°) was placed in front of a scintillation Xe-detector. The data were collected with 2θ angle varying from 30° to 148° in a continuous scan, using step of 0.05° with an integration time of 10 s/step. The shape of diffraction peaks were corrected for Lorentz-Polarisation factor as well for absorption effect using appropriate formulas for MGIXD as well as for symmetric omega-two theta scan, given in [27,28]. The pseudo-Voigt profiles (taking into account $K\alpha_1+K\alpha_2$ doublet) with linear background approximation were fitted to well defined and good quality peaks in order to determine their 2θ positions.

A sample suitable for tensile test, shaped like a dog's bone, with an effective length of 15 mm, width of 4.9 mm, and thickness of 0.6 mm, was machined from the received ingot of Ti-18. The longitudinal axis of the sample was parallel to the axial direction of the ingot. The sample was mechanically and electrically polished (in a solution A3 produced by Struers) in order to avoid the influence of surface heterogeneities. During electro-polishing of the samples more than 20 μm of the material was removed.

To characterise the crystallographic texture in both phases of the studied Ti alloy, two sets of pole figures, i.e. $\{0002\}_\alpha$, $\{1100\}_\alpha$, $\{1101\}_\alpha$, $\{1102\}_\alpha$ and $\{110\}_\beta$, $\{002\}_\beta$, $\{211\}_\beta$, were measured for α - and β -phases, respectively. The intensities of pole figures were measured at the nodes of a grid with step of 5° for tilt and azimuth angles, within the ranges from 0° to 65° and from 0° to 360° , respectively. Subsequently, the orientation distribution functions (ODFs, given in Fig. 3) were determined for each phase using the WIMV method [33]. The

TKD and X-ray diffraction measurements showed that lattice orientation in both α_p and α_s precipitates fulfils or they are very close to the Burgers relation $\{110\}_\beta || \{0002\}_\alpha$ [1].

A series of X-ray diffraction measurements were carried out during *in-situ* uniaxial tensile test following the stabilisation of applied loads for constant sample strains E_{11} . The true stress (Σ_{11}^{mech} - stress applied to the sample) for each measuring point was calculated, accounting for the cross-sectional decrease during plastic deformation, from the applied force, measured by load cell. The true strain (E_{11}) of the sample was calculated from measured displacements of the grip (accounting for machine stiffness and assuming the known Young's modulus of Ti alloy, equal to 110 GPa [18]). Measurements were performed for the initial sample, the sample under external loaded stress Σ_{11}^{mech} , and the sample after fracture (e.g. for the unloaded sample). To distinguish different types of stresses and strains defined in this paper the meaning of different symbols are summarised in Table 3.

The stress state in the near-surface volume was determined independently for α - and β -phases of the Ti alloy using the MGIXD method [20-28]. As illustrated in Fig. 4, this method is based on asymmetric diffraction geometry in which a small incident angle α is kept constant during measurement and the interplanar spacings $\langle d^\Sigma \rangle_{\{hkl\}}$ are measured for different hkl reflections, corresponding to different orientations of the scattering vector indicated by the $\psi_{\{hkl\}}$ angle [20,24-27]:

$$\psi_{\{hkl\}} = \theta_{\{hkl\}} - \alpha \quad (1)$$

where $\psi_{\{hkl\}}$ is the angle between the scattering vector and a surface normal to the sample and $2\theta_{\{hkl\}}$ is the scattering angle.

During the measurements, the incident angle $\alpha = 10^\circ$ was kept constant; thus the stress state was studied at a constant penetration depth of about 1.6 μm . The measurements were carried out by inclining the scattering vector first between normal to the sample surface and

loading direction ($\phi = 0^\circ$), and next between the normal and transverse directions ($\phi = 90^\circ$), where the angle ϕ characterises the rotation around normal to the surface. It should be emphasised that in this experiment the penetration depth of X-rays (1.6 μm) is much smaller than the size of grains (especially in the case of α_p precipitates, cf. Fig.1), however in the case of MGIXD method large surface of the sample (approximately 5 mm x 8 mm for incident angle $\alpha = 10^\circ$) was irradiated by the incident beam. This leads to very good statistic of measured grains (about 10^6 precipitates of α_p precipitates) and good representativity of the experimental data. The mechanical behaviour of the near surface volume at similar depths were previously studied using MGIXD for the *in situ* loaded austenitic [26, 27] and Ti samples [27]. The results presented in those works show a good agreement between macrostresses applied to the sample and these measured by diffraction, within elastic range of deformation. It should be however noted that in the case of very shallow depths only the part of the grains close to the free surface is seen using MGIXD, thus we can assume that the forces/stresses normal to the surface relaxes in this volume. Taking into account small ratio of the penetration depth to the grain size we can expect that the 33 component of macroscopic stress tensor is equal to zero not only for the macrostresses (as usually in the case of X-ray measurements) but also for intergranular incompatibility stresses. Therefore, the influence of plastic incompatibility stresses on the determined lattice strains also decreases.

To interpret the results obtained using the MGIXD method, it is beneficial to define the equivalent lattice parameter $\langle a(\phi, \psi) \rangle_{\{hkl\}}$, which is expressed by the macrostresses σ_{ij} and the strain-free lattice constant a_0 [16–21]:

$$\langle a(\phi, \psi) \rangle_{\{hkl\}} = [F_{ij}(hkl, \phi, \psi) \sigma_{ij}] a_0 + a_0 \quad (2)$$

where, for the cubic crystal structure: $\langle a(\phi, \psi) \rangle_{\{hkl\}} = \langle d(\phi, \psi) \rangle_{\{hkl\}} \sqrt{h^2 + k^2 + l^2}$, (2a)

or for the hexagonal structure: $\langle a(\phi, \psi) \rangle_{\{hkl\}} = \langle d(\phi, \psi) \rangle_{\{hkl\}} \left\{ \left[\frac{4}{3}(h^2 + hk + k^2) \right] + \frac{l^2}{(c/a)^2} \right\}^{1/2}$, (2b)

and where $F_{ij}(hkl, \phi, \psi)$ are the X-ray stress factors (XSFs).

The σ_{ij} and a_0 fitting parameters can be found by adjusting the $\langle a(\phi, \psi) \rangle_{\{hkl\}}$ values obtained from Eq. 2a or b to the measured values (Eq. 2). However, in principle, the exact value of the c/a parameter is unknown for hexagonal alloys; in this case, the iteration method proposed in [20] is applied.

It should be noted that in many previous works an additional term responsible for second order incompatibility stress was added to Eq. 2 and used to determine these stresses from nonlinearities in the $\langle a(\phi, \psi) \rangle_{\{hkl\}}$ vs $\sin^2\psi$ curve, as proposed by Baczmanski et al. [34,35]. Also, Gloaguen et al. [23] successfully used this additional term in MGIXD method to determine plastic incompatibility stresses in rolled Zircaloy-4. However, in the present work the additional term responsible for second order stresses was neglected because the nonlinearities observed in the case of studied Ti-18 material are small (contrary to a significant effect shown for rolled Zircaloy-4 in [23]) and also due to the arguments given in section 3.3, where the results of measurements are discussed.

Additionally, for each applied load Σ_{11}^{mech} , the relative lattice strains $\langle \varepsilon_{33} \rangle_{\{hkl\}}^{ph}$ in a direction perpendicular to the load (with respect to the initial interplanar spacings) were determined for different hkl reflections in both phases using symmetric $\theta-2\theta$ geometry (the scattering vector was normal to the surface, i.e. $\psi_{\{hkl\}} = 0$):

$$\langle \varepsilon_{33} \rangle_{\{hkl\}}^{ph} = \frac{\langle d^\Sigma \rangle_{\{hkl\}} - \langle d^0 \rangle_{\{hkl\}}}{\langle d^0 \rangle_{\{hkl\}}} \quad (3)$$

where $\langle d^\Sigma \rangle_{\{hkl\}}$ and $\langle d^0 \rangle_{\{hkl\}}$ are the interplanar spacings of the $\{hkl\}$ planes measured for the sample under an applied uniaxial macroscopic load Σ_{11}^{mech} and without external load (initial state), respectively.

3. Results and discussion

3.1 Model calculations

In order to interpret the experimental results, the prediction of elasto-plastic deformation was made with the self-consistent model [11,29], using 40,000 spherical inclusions, of which 18,000 represent α -phase (45%) and 22,000 β -phase crystallites (55%). The initial crystallographic textures (Fig. 3) of each phase were used to determine the crystallites' initial orientations. The crystalline structures of each phase and SECs were taken into account in the calculations (Table 1). Initial stress was equal to zero for each inclusion because (as it will be shown later) these stresses relax when the slip systems are activated in α -phase. To predict the plastic deformation of a grain, glides on the slip systems were conducted, but the twinning phenomenon was not considered for any phase in this simulation, according to the results of our microstructural studies (cf. Fig. 2) and the literature reports [1,8,15-17]. The aim of this work was to identify initial CRSS (τ_0^{ph}) and initial hardening of the slip system (H_0^{ph}) [11,29] for each phase (ph), during small sample strain up to $E_{11} \approx 4.5\%$. In calculations, the virtual tensile loading was applied in the same direction as in the experiment (i.e. along LD – loading direction; see Fig. 4) and the parameters were adjusted in order to reproduce the experimental results as closely as possible.

3.2 Lattice strain evolution compared with model prediction

The measured relative elastic lattice strains (Eq. 3) in the direction normal to the surface (ND) were compared with the model predictions, as presented in Fig. 5. For the calculations, the single crystal elastic constants shown in Table 1 for α - and β -phases were used. In the case of β -phase different sets of SECs found in literature were tried. It was found that an excellent agreement between experimental and model lattice strains were obtained for both phases, only when the SECs of β -phase, exhibiting the lowest value of anisotropy factor (Zener factor $A = 1.4$ for Ti-17 alloy), were used in prediction of elastic and plastic deformation (see Fig. 5 a). In Fig. 5 b it was shown that for higher elastic anisotropy of SECs for β -phase, the model lattice strains (in this phase) cannot be fitted to experimental points

due to large differences in elastic responses predicted for different reflections hkl (especially for 200 and 310 reflections). In contrast, the experimental lattice strains for the studied Ti-18 alloy are almost equal for various hkl reflections during the whole range of elastic and plastic deformation. It can be concluded that the SECs of β -phase, previously determined for Ti-17 [18], correctly describe elasticity of this phase within the Ti-18 alloy subjected to precipitation hardening thermal treatment. This conclusion agrees well with the results presented in [17], where a significant dependence of the anisotropy of SECs on treatment temperature was shown for β -phase in Ti-10V-2Fe-3Al alloy. The significant anisotropy was confirmed by evolution of lattice strains calculated and measured during tensile test for forged material, while in the aged alloy the SECs for β -phase exhibited much lower anisotropy. In the present work the SECs of β -phase from Ti-17 alloy will be used [18] for further model predictions as well as to calculate XSFs used in Eq. 2.

In the range of plastic deformation, the best agreement between model and experiment was obtained for both phases (Fig. 5 a) with the parameters given in Table 4. For bcc phase the same value of CRSS was adjusted for operating pencil glide slip systems [1]. In the case of α phase the activation of slip system is more complex due to different CRSS values for different slip systems, smaller number of symmetrically equivalent slips, as well as different stresses localized in the grains having various orientations. We present the solution for the optimum fitting of all curves; however, it has not been proved that this solution is unique. Comparing results of model prediction with experimental data for different sets of CRSS in α -phase, the smallest value of CRSS for B<a> slip was found, while the other values were higher and approximately equal to each other. In spite of not enough sensitivity to find out the exact relations between CRSS values for slip systems within each phase, the performed analysis satisfactorily determines relation between CRSS in different phases. This is done due to phase selectivity of diffraction method used for lattice strain measurements. It was found

that the CRSS in both phases are similar but the values for the α -phase are slightly smaller. It should be also mentioned that, using the model, we confirmed that, especially in the case of β -phase, crystallographic texture plays an important role in the activation of slip systems.

As discussed in [17] the relations between the CRSS values in α - phase are different for single and two phase Ti alloys. In the case of single α - phase titanium the $\langle c + a \rangle$ slips are few times harder than prismatic and basal $\langle a \rangle$ slips [1-7]. Because activation of $\langle a \rangle$ systems is not enough to allow full plastic deformation of a grain, the usually much harder $\langle c + a \rangle$ slips or twinning are required to start plastic deformation of polycrystalline material. However, the anisotropy of slips systems (caused by difference between CRSSs for $\langle c + a \rangle$ and $\langle a \rangle$ slips) decreases in the case of two phase alloys, as seen in the case of the studied Ti-18 alloy. This effect depends on the alloy composition [14-17] as well as thermal treatment subjected to the sample [17]. As shown in [14-17] also the difference between CRSS values for β -phase and α -phase depends on the composition and thermal treatment, and usually α -phase is harder than β -phase. However, after aging a significant hardening of β -phase lead to smaller difference between CRSSs for both phases [17]. In the studied Ti-18 alloy, the CRSS values of β -phase are slightly higher than these of α -phase, which leads to a strengthening of the whole material which is superior in comparison with previously studied two phase Ti-alloys [14-17].

The evolutions of average lattice strains $\langle \varepsilon_{33} \rangle^{ph}$ calculated independently from all available hkl reflections for each phase are shown in Fig. 6. It can be seen that the elastic lattice strains in the ND are negative for both phases (effect of Poisson ratio or lateral contraction in the elasto-plastic range) and two thresholds representing limits of elastic deformation limits for each phase (A and B) can be found on the plots presented in Fig. 6. These thresholds were set at the ends of linear ranges of the average lattice strains $\langle \varepsilon_{33} \rangle^{ph}$ vs sample strain E_{II} plots predicted by model. It should be emphasised that the model

prediction is an optimal one for which the best agreement with experiment was obtained for all lattice strains $\langle \varepsilon_{33} \rangle_{\{hkl\}}^{ph}$ presented in Fig. 5a. At the beginning of the tensile test, linear evolution of negative lattice strains occurs until the thresholds A for α -phase and B for β -phase are reached. This corresponds to the elastic deformation stage of the considered phases during the tensile test. In the interval between thresholds A and B , plasticity of α -phase occurs, while β -phase remains elastic. Finally, after threshold B , both phases undergo plastic deformation and the evolution of both curves shows saturation with small work hardening described by parameters H_0^{ph} [11,29] given in Table 4. In model prediction an isotropic hardening was assumed, i.e. the self-hardening and latent hardening terms [11,29] were equal to the same value H_0^{ph} defined for all systems in a given phase. This simplest assumption allows to predict correctly the slopes of different lattice strains $\langle \varepsilon_{33} \rangle_{\{hkl\}}^{ph}$ vs sample strain E_{11} in the plastic range of deformation, as shown in Fig. 8. Only the initial hardening was determined, because the sample was fractured at a small macrostrain E_{11} of about 4.5%. A similar approximation reducing significantly the number of undistinguishable parameters was used in [17] where in model calculations identical and isotropic hardening was assumed for all systems in both phases. In that work, the value of initial hardening rate (parameter of Voce law $\theta_0 = 10$ MPa) obtained for the aged Ti-10V-2Fe-3Al alloy is also close to the results obtained in the present work (Table 4). In other studied alloys different hardening parameters (usually much higher) were determined or assumed for different slip systems [14-16]. However, it was not proved or even discussed that the presented solutions with a large number of adjusted unknown parameters are unique.

Finally, Fig. 7a shows the mean values of accumulated shear strain for slip systems operating in one grain:

$$\text{accumulated shear strain} = \frac{1}{N} \sum_{\{hkl\}} \langle uvw \rangle \gamma \quad , \quad (4)$$

where the sum of slip amplitudes (i.e. γ shear strains) $\sum_{\{hkl\} \langle uvw \rangle} \gamma$ is calculated for a given slip system $\{hkl\} \langle uvw \rangle$ (in the case of hcp lattice $\{hkil\} \langle uviw \rangle$) for all grains and N is a number of grains.

Additionally, the sum of accumulated shear strain for all systems and systems in each phase is presented in Fig. 7b.

By analysing Fig. 7, the history of slip system activation can be described. The first activated system is the prismatic system P $\langle a \rangle$ (see Table 4 and threshold A at about 850 MPa in Fig. 7). Next, around $\Sigma_{II} = 950$ MPa, basal B $\langle a \rangle$ and pyramidal III $\langle c+a \rangle$ slips begin to be active. In the range from A to B a small macroscopic plastic deformation occurs because only slip systems in α -phase are active, while the β -phase remains elastic. The successive pencil glide (three slip systems, cf. Table 4) in bcc β -phase and the slip system III $\langle a \rangle$ in hcp α -phase are activated above the macroscopic stress $\Sigma_{II} = 1050$ MPa, leading to significant plasticity of the material above the B threshold (cf. Fig. 7).

3.3 Experimental phase stresses and model prediction

Given the very shallow penetration depth of X-rays in the MGIXD measurements, we can assume that the stress relaxes in the direction normal to the surface, leading to the assumption $\sigma_{33}^{ph} = 0$. Therefore, the stresses σ_{11}^{ph} and σ_{22}^{ph} in both phases can be independently determined. In the case of hexagonal α -phase, the analysis of experimental data was based on a methodology in which the value of the c/a parameter was adjusted, as proposed recently by Marciszko et al. [24]. The XSFs in Eq. 2 were calculated using the Eshelby-Kröner [21,35-37] model from the SECs given in Table 1, accounting for the crystallographic textures shown in Fig. 4. In the case of β -phase the SECs from the Ti-17 alloy were used. It was also checked that the influence of model type used to calculate XSF is not significant. Comparison between example stress determined with Eshelby-Kröner with model and extreme Voigt and

Reuss approaches [21,37] shown differences less than 4% for α -phase and about 1% for β -phase. Also, the influence of texture was not large, i.e. difference between σ_{11}^{ph} stresses calculated from Eq. 2 assuming quasi-isotropic sample (without texture) and accounting for ODFs shown in Fig. 4 is about 3% for α -phase and 7% for β -phase. The most significant variation was obtained when calculating XSFs from different SECs found in literature for β -phase within two phase Ti alloys. Thus, several sets of SEC proposed in the literature were used to compute average phase stresses and macrostresses from measured strains. These averaged stresses were then compared to the applied macrostress as obtained with the load cell. Table 5 shows the example of a macrostress of 1211 MPa.

It can be seen that a good agreement between the macrostress measured by diffraction (Σ_{11}^{diff}) and the one applied to the sample (Σ_{11}^{mech}) was achieved when the SECs of β - phase in Ti-17 alloy [18] were used to calculate XSFs and to determine phase stresses from Eq. 2. As shown in Table 5, much worse agreements between Σ_{11}^{diff} and Σ_{11}^{mech} stresses were obtained when others sets of SECs were used in stress analysis. It is important to note, that the above test for the SECs verification is based directly on stress analysis without any comparison with self-consistent prediction (as in section 3.2 and for example in [14]). We can conclude that independent verification procedure confirmed that previously chosen SECs of β - phase from Ti-17 alloy correctly characterise elastic properties of β - phase within Ti-18 alloy and these SECs were used in further analysis.

The example fitting results (using Eq. 2) for both phases and two ϕ angles (0° and 90°) are presented in Fig. 8, where the $\langle a(\phi, \psi) \rangle_{\{hkl\}}$ vs $\sin^2 \psi$ plots are shown for three different states during the tensile test. The first pair of figures presents the results obtained for α - and β -phases, respectively, in the initial sample, without tensile loading. Next, the analogical plots are shown for the plastically deformed sample (under loading: $\Sigma_{11} = 1211$ MPa) and finally for the unloaded (fractured) sample. All curves are nearly linear, with relatively small

deviations. The significant slope of the plots measured in the direction of applied load ($\phi = 0^\circ$) for $\Sigma_{11}^{mech} = 1211$ MPa indicates large tensile stresses in both phases. The experimental results (points) are correctly adjusted through least-squares minimisation (lines), using Eq. 2. No significant spread of experimental points around the lines is observed in the initial material, under applied load, or after unloading/fracture of the sample.

In the initial sample biaxial phase stresses were determined: $\sigma_{11}^{\alpha} = -37 \pm 64$ MPa, $\sigma_{22}^{\alpha} = -35 \pm 65$ MPa and $\sigma_{11}^{\beta} = 118 \pm 56$, $\sigma_{22}^{\beta} = 89 \pm 56$. These stresses are generated probably due to relatively smaller contraction of β - phase (coefficients of thermal expansion CTE for crystallite: $\alpha_{11} = \alpha_{22} = \alpha_{33} = 8.3 \cdot 10^{-6} \text{ K}^{-1}$ [15]) in comparison to α - phase ($\alpha_{11} = \alpha_{22} = 9.3 \cdot 10^{-6} \text{ K}^{-1}$ and $\alpha_{33} = 8.7 \cdot 10^{-6} \text{ K}^{-1}$ [15]) during sample cooling from precipitation hardening temperature to room temperature. The phase stresses exhibit biaxial character because in the near-surface region the σ_{33}^{ph} stress relaxes. For α - phase crystals, as discussed in [15], the difference between CTE in the direction parallel to basal crystallographic plain and direction along c axis can introduce additional incompatibility stresses. The effect of these stresses should be seen as a spread of experimental points around the fitted lines in Fig. 8a, and this spread should be modified by the plastic incompatibility stresses produced during plastic deformation [23]. However, the deviations of experimental points from the fitted $\langle a(\phi, \psi) \rangle_{\{hkl\}}$ vs $\sin^2 \psi$ lines did not changed significantly after tensile test (cf. plots for initial and unloaded sample in Fig. 8 for both phases). This means that small disagreements between experiment and theoretical lines are not really caused by intergranular stresses but they result from experimental uncertainties, approximations made in calculation of XSF or other effects which do not changed during plastic deformation. The reasons for the insignificant values of incompatibility stresses are probably a small total sample strain

(fracture at about $E_{11} \approx 4.5\%$) and the fact that measurements were made close to the surface as discussed in section 2.

We can conclude that the incompatibility stresses within each phase are small and can be neglected when calculating the mean phase stresses. Moreover, the linear character of the $\langle a(\phi, \psi) \rangle_{\{hkl\}}$ vs $\sin^2 \psi$ plots indicates no presence of shear stresses σ_{13}^{ph} and σ_{23}^{ph} in the gauge volume analysed using X-rays. Due to the nearly orthorhombic symmetry of the texture (Fig. 3) and the symmetrical character of tensile load, the shear stress component σ_{12}^{ph} is also negligible. Therefore the determined biaxial stress state (σ_{11}^{ph} and σ_{22}^{ph} components) completely describes the stress state in both phases.

Fig. 9 shows the comparison between the stresses σ_{11}^{ph} and σ_{22}^{ph} (along the loading direction LD and transverse direction TD) in each phase determined using the MGIXD method (section 2.2) and the corresponding model stresses predicted using the parameters given in Table 4. In Fig. 9 the stress evolutions in both phases are presented vs sample strain E_{11} . Taking into account the uncertainties of the measurements, it can be stated that good agreement between measured and predicted phase stresses σ_{11}^{ph} and σ_{22}^{ph} was obtained (see Fig. 9a and b). In Fig. 9, the yield point of each phase is indicated by thresholds A and B , referring to the activation of slip systems (cf. Fig. 6). We can see that initially both phases exhibit linear behaviour (vs sample strain E_{11}) during elastic deformation. The model lines are slightly shifted with respect to the measured points because of small initial inter-phase experimental stresses, which were not taken into account in calculations. Within the range between A and B , two slips are activated successively in α -phase, which does not lead to significant softening of any phase (Fig. 9a), i.e. these glides are not sufficient to induce macroscopic plasticity of the material. Also, it should be pointed out that some fluctuation of the determined stress in β -phase was observed at about $\Sigma_{11} \approx 800 - 1000$ MPa, which can

be caused by a relaxation of the initial interphase stresses (cf. Fig. 9b). Above this range a good agreement between experiment and model was obtained because the model calculations were performed neglecting initial stresses. Finally, the activation of all slips in β -phase and $B\langle a \rangle$ in α -phase occurring above point B (Σ_{11} between 1050 MPa and 1100 MPa) led to the initiation of plastic deformation in both phases. The last measurement, carried out after sample fracture, showed residual phase stresses σ_{11}^{α} and σ_{11}^{β} with opposite signs, and a similar stress state of the material was also predicted by the self-consistent model (Fig. 9). Unlike model stresses, experimental phase results show an absolute value of σ_{11}^{β} much greater than σ_{11}^{α} , it means that, in the actual sample, an additional residual macrostress was generated (see also Fig. 10).

The evolution of overall mechanical stress Σ_{11}^{mod} vs strain E_{11} , determined using three independent approaches, is presented in Fig. 10a and b. The first plots, i.e. Σ_{11}^{diff} and Σ_{22}^{diff} vs E_{11} show the macrostresses determined as the volume-weighted mean values from the phase stresses measured using MGIXD; the second plot Σ_{11}^{mod} vs E_{11} was obtained using the self-consistent model for the parameters given in Table 4; and the final plot Σ_{11}^{mech} vs E_{11} shows the mechanical true macroscopic stress determined from the data recorded by the load cell. It was found, that since no load was applied to the sample in the TD direction, the Σ_{22}^{diff} stress was approximately equal to zero (within the uncertainty range) during the entire tensile test. Linear behaviour of Σ_{11} vs E_{11} plots can be observed in all of the presented plots during the elasticity stage up to threshold A . Within this range, the results obtained using the diffraction method and recorded by the tensile rig are in good agreement (Fig. 10a). A small decrease in overall stress was determined for Σ_{11}^{diff} using MGIXD, when the $P\langle a \rangle$ slip system was activated ($\Sigma_{11} \approx 850$ MPa, Fig. 10b). This kind of fast step relaxation

occurs only in the gauge volume measured by diffraction and is not observed in the macroscopic response Σ_{11}^{mech} vs E_{11} (Fig. 10b). Thus, the reason for the latter evolution can be explained by the effect of sample heterogeneity, such as microdamage or cracking in the near-surface region of the sample. It was observed that the surface stress (i.e. Σ_{11}^{diff}) was smaller than the mean stress in the bulk volume (Σ_{11}^{mech}), which means that the deformation was not homogenous over the cross section of the sample. However, such heterogeneity is not very significant because the difference between Σ_{11}^{diff} and Σ_{11}^{mech} did not exceed 10%.

After the small step relaxation, the macroscopic stress Σ_{11}^{diff} rises again with an increasing rate (slope) almost equal to that during elastic deformation (Fig. 10a, b). Significant macroscopic plastic deformation was initiated above 1050 MPa (B threshold) along with the activation of the slip systems in β -phase. The latter phenomenon is clearly confirmed by the evolution of the model-predicted overall stress Σ_{11}^{mod} . Finally, we can see that after sample fracture, i.e. after sample unloading (i.e. $\Sigma_{11}^{mech} = 0$), a small non-zero compressive residual stress (i.e. $\Sigma_{11}^{diff} < 0$) remained on the sample's surface.

4. Summary

For the first time, the MGIXD method was applied to a study of the micromechanical behaviour of the phases/aggregates in polycrystalline material. This methodology has many advantages in comparison with the frequently used neutron or synchrotron transmission methods. One of the most important features of this method is its capacity for stress determination in a well-defined near-surface volume, where the normal stress is relaxed. This enables the direct measurement of other stress components in the initial sample, as well as throughout the loading process. In this case, the measured stresses yield new information thanks to which the elasto-plastic transition can be directly observed for each phase. For instance, in this study we found that both phases remained almost elastic in spite of the

activation of some slip systems in α -phase. This effect can be observed if the stresses in both phases are measured directly. Another advantage of MGIXD is that many hkl reflections can be recorded during stress measurement. From the experimental $\langle a(\phi, \psi) \rangle_{\{hkl\}}$ vs $\sin^2\psi$ curves we can easily determine whether or not intergranular stresses (deviations from the mean phase stresses) play an important role in the studied sample. The linearity of these curves shows that the magnitude of intergranular stresses is negligible with respect to first-order stresses. The final advantage of this presented methodology is that the experiment can be performed using a laboratory diffractometer in reflection mode. The most important inconvenience of the MGIXD method is that only the state of near-surface stresses can be analysed, and results of this kind may not be representative of heterogeneous samples. However, in our experiment the difference between overall and surface stress in the bulk material was less than 10%.

As a result of the analysis performed in this work, the appropriate SECs for β -phases were chosen and verified using two independent tests based on the measurements of lattice strains direction in normal to the surface, as well as stresses in each phase (MGIXD). It was shown that the hcp crystallites in aged samples exhibit low elastic anisotropy and this behaviour is confirmed by the literature. Moreover, the initial CRSS values for different slip systems in α - and β -phases in Ti-18 alloy was determined by comparing the lattice strains with the predictions of the self-consistent model. Very good agreement between measured and predicted data confirms the reliability of the determined values of CRSS. It was found that slip systems are initially activated in α -phase. Subsequently, the measured phase stresses and macrostresses were compared with theoretical values and good agreement within the range of uncertainty was obtained. Analysis of the latter results showed that in spite of earlier activated slips in α -phase, both phases remain almost elastic until the activation of slips in β -phase. The role of α_p and α_s precipitates in plastic deformation of the alloy can be

investigated on the basis of the TKD results. As shown in Fig. 2, the lamellas of the secondary phase are much smaller and more densely distributed in comparison with α_p grains. Thus, it can be supposed that the α_s lamellas create barriers for dislocation mobility leading to high values of CRSS for slips in the matrix, which consists of β phase with embedded α_s lamellas. This can be a reason for relatively high values of the CRSS in β -phase.

Acknowledgements. The work was supported partly by the Regional Council of Champagne-Ardenne (Conseil Régional de Champagne-Ardenne); NCN (National Science Centre, Poland) grants nos. UMO-2014/15/D/ST8/00542 and UMO - 2011/03/N/ST8/04058; and the MNiSW (Polish Ministry of Science and Higher Education).

REFERENCES:

- [1] G. Lütjering, J. C. Williams, Titanium, 2nd edition, Springer, 2007.
- [2] M.J. Philippe, M. Serghat, P. Van Houtte, C. Esling, Modelling of texture evolution for materials of hexagonal symmetry – II Application to zirconium and titanium α or near α alloys, Acta Metall. Mater. 43 (1995) 1619–1630.
- [3] N. Benmhenni, S. Bouvier, R. Brenner, T. Chauveau, B. Bacroix, Micromechanical modelling of monotonic loading of CP α -Ti: Correlation between macroscopic and microscopic behavior, Mat. Sci. Eng. A 573 (2013) 222–233.
- [4] C. Zambaldi, Y. Yang, T. R. Bieler, D. Raabe, Orientation informed nanoindentation of alpha-titanium: Indentation pileup in hexagonal metals deforming by prismatic slip, J. Mater. Res. 27 (2012) 356-367.
- [5] D. Gloaguen, G. Oum, V. Legrand, J. Fajoui, S. Branchu, Experimental and theoretical studies of intergranular strain in an alpha titanium alloy during plastic deformation, Acta Mater. 61 (2013) 5779- 5790.

- [6] D. Gloaguen, G. Oum, V. Legrand, J. Fajoui, M.-J. Moya, T. Pirling, W. Kockelmann, Intergranular Strain Evolution in Titanium During Tensile Loading: Neutron Diffraction and Polycrystalline Model, *Metall. Mater. Trans. A* 46 (2015) 5038-5046.
- [7] B. Barkia, V. Doquet, J.P.Couzinié, I.Guillot, E.Héripré, In situ monitoring of the deformation mechanisms in titanium with different oxygen contents, *Mat. Sci. Eng. A* 636 (2015) 91-102.
- [8] D. G. Leo Prakash, R. Ding, R.J. Moat, I. Jones, P.J. Withers, J. Quinta da Fonseca, M. Preuss, Deformation twinning in Ti-6Al-4V during low strain rate-moderate strains at room temperature, *Mat. Sc. and Eng. A* 527 (2010) 5734–5744.
- [9] B. Clausen, T. Lorentzen, M.A.M. Bourke, M.R. Daymond, Lattice strain evolution during uniaxial tensile loading of stainless steel, *Mater. Sci. Eng. A* 259 (1999) 17–24.
- [10] S. Cai, M.R. Daymond, R.A. Holt, Modeling the room temperature deformation of a two phase zirconium alloy, *Acta Mater.* 57 (2009) 407–419.
- [11] A.Baczmański, Y. Zhao, E. Gadalińska, L. Le Joncour, S. Wroński, C. Braham, B. Panicaud, M. François, T. Buslaps, K. Soloducha M., Elastoplastic deformation and damage process in duplex stainless steels studied using synchrotron and neutron diffractions in comparison with a self-consistent model, *Int. J. Plasticity* 81 (2016) 102–122.
- [12] N. Jia, Z.H. Cong, X. Sun, S. Cheng, Z.H. Nie, Y. Ren, P.K. Liaw, Y.D. Wang, An in situ high energy X-ray diffraction study of micromechanical behavior of multiple phases in advanced high-strength steels, *Acta Mater.* 57 (2009) 3965–3977.
- [13] M.L. Young, J.D. Almer, M.R. Daymond, D.R. Haeffner, D.C. Dunand, Load partitioning between ferrite and cementite during elasto-plastic deformation of an ultrahigh-carbon steel, *Acta Mater.* 55 (2007) 1999–2011.

- [14] V. Hounkpati, S. Freour, D. Gloaguen, V. Legrand, J. Kelleher, W. Kockelmann, S. Kabra, In situ neutron measurements and modelling of the intergranular strains in the near- β titanium alloy Ti- β 21S, *Acta Mater.* 109 (2016) 341-352.
- [15] J.L.W. Warwick, J. Coakley, S.L. Raghunathan, R.J. Talling, D. Dye, Effect of texture on load partitioning in Ti-6Al-4, *Acta Mater.* 60 (2012) 4117-4127.
- [16] A.M. Stapleton, S.L. Raghunathan, I. Bantounas, H.J. Stone, T.C. Lindley, D. Dye, Evolution of lattice strain in Ti-6Al-4V during tensile loading at room temperature, *Acta Mater.* 56 (2008) 6186-6196.
- [17] S.L. Raghunathan, A.M. Stapleton, R.J. Dashwood, M. Jackson, D. Dye, Micromechanics of Ti-10V-2Fe-3Al: In situ synchrotron characterisation and modeling, *Acta Mater.* 55 (2007) 6861-6872.
- [18] S. Freour, D. Gloaguen, M. François, A. Perronnet, R. Guillen, Determination of single-crystal elasticity constants in a cubic phase within a multiphase alloy: X-ray diffraction
- [19] C.-E. Hu, Z.-Y. Zeng, L. Zhang, X.-R. Chen, L.-C. Cai, D. Alfe, Theoretical investigation of the high pressure structure, lattice dynamics, phase transition, and thermal equation of state of titanium metal, *J. Appl. Phys.* 107 (2010) 093509.
- [20] S. J. Skrzypek, A. Baczmanski, W. Ratuszek and E. Kusior, New approach to stress analysis based on grazing-incidence X-ray diffraction, *J. Appl. Cryst.* 34 (2001) 427-435.
- [21] U. Welzel, J. Ligot, P. Lamparter, A. C. Vermeulen and E. J. Mittemeijer, Stress analysis of polycrystalline thin film and surface regions by X-ray diffraction, *J. Appl. Cryst.* 38 (2005) 1-29.
- [22] Ch. Genzel, X-ray residual stress analysis in thin films under grazing incidence – basic aspects and applications, *Mater. Sci. Technol.* 21 (2005) 10-18.

- [23] D. Gloaguen, J. Fajoui, B. Girault, Residual stress fields analysis in rolled Zircaloy-4 plates: Grazing incidence diffraction and elastoplastic self-consistent model. *Acta Mater.* 71 (2014) 136–144.
- [24] M. Marciszko, A. Baczmański, C. Braham, M. Wróbel, W. Seiler, S. Wroński and K. Berent, Analysis of stresses and crystal structure in the surface layer of hexagonal polycrystalline materials: a new methodology based on grazing incidence diffraction. *J. Appl. Cryst.*, 49 (2016) 85-102.
- [25] M. Marciszko, A. Baczmański, C. Braham, M. Wróbel, S. Wroński, G. Cios, Stress measurements by multi-reflection grazing-incidence X-ray diffraction method (MGIXD) using different radiation wavelengths and different incident angles, *Acta Mater.*, 123 (2017) 157–166.
- [26] M. Marciszko, A. Baczmański, M. Wróbel, W. Seiler, C. Braham, S. Wroński, R. Wawszczak, Problem of elastic anisotropy and stacking faults in stress analysis using multireflection grazing-incidence X-ray diffraction, *J. Appl. Cryst.*, 48 (2015) 492–509.
- [27] M. Marciszko, Diffraction study of mechanical properties and residual stresses resulting from surface processing of polycrystalline materials, PhD Thesis, AGH, Kraków, 2013, <http://winntbg.bg.agh.edu.pl/rozprawy2/10658/full10658.pdf>
- [28] S. Wroński, K. Wierzbanowski, A. Baczmański, A. Lodini, C. Braham, W. Seiler, X-ray grazing incidence technique—corrections in residual stress measurement- a review, *Powder Diffr. Suppl.*, 24 (2009) S1-S15.
- [29] P. Lipinski, M. Berveiller, E. Reubrez, J. Morreale, Transition theories of elastic-plastic deformation of metallic polycrystals, *Arch. Appl. Mech.* 65 (1995) 291–311.
- [30] E. Lebrun, P. Svec, S. Nowak, B. Denand, Y. Millet, F. Prima, Phase transformations of TIMETAL-18 as a new titanium alloy with bimodal microstructure, *Adv. Mater. Research* 922 (2014) 418-423.

- [31] P. W. Trimby, Orientation mapping of nanostructured materials using transmission Kikuchi diffraction in the scanning electron microscope, *Ultramicroscopy* 120 (2012) 16–24.
- [32] T. Tokarski, G. Cios, A. Kula, P. Bała, High quality transmission Kikuchi diffraction analysis of deformed alloys - Case study, *Mater. Character.* 121 (2016) 231–236.
- [33] J.S. Kallend, U.F. Kocks, A.D. Rollet, H.R. Wenk, *Operational Texture Analysis*. Rap. LA-UR-90e2852. CMS, Los Alamos National Laboratory, USA, 1990.
- [34] S. Wroński, A. Baczański, R. Dakhlaoui, C. Braham, K. Wierzbowski, E.C. Oliver, Determination of Stress Field in Textured Duplex Steel Using TOF Neutron Diffraction Method, *Acta Mater.* 55(2007) 6219-6233.
- [35] A. Baczański, P. Lipiński, A. Tidu, K. Wierzbowski, B. Pathiraj, Quantitative estimation of incompatibility stresses and elastic energy stored in ferritic steel, *J. Appl. Cryst.*, 41 (2008) 854-865.
- [36] F. Bollenrath, V. Hauk, E.H. Müller: Zur Berechnung der vielkristallinen Elastizitätskonstanten aus den Werten der Einkristalle, *Z. Metallkde.* 58 (1967) 76-82.
- [37] V. Hauk, *Structural and Residual Stress Analysis by Nondestructive Methods*, Elsevier, Amsterdam, 1997.

FIGURE CAPTIONS:

Fig. 1. SEM images showing the microstructure of Ti-18 in radial cross sections.

Fig. 2 . Results of TKD measurement for initial (a) and deformed (b) samples: lamellar structure of α_s phase embedded in β phase (on the left) and α_p precipitates (on the right) are shown (IPF – inverse pole figure, IQ – image quality index and Phase map).

Fig. 3. ODFs for both phases of the studied Ti alloy, determined using X-ray diffraction. The sample orientation was defined by: x_1 – applied load direction (LD), x_2 – transverse direction (TD), and x_3 – normal direction (ND). Sections through Euler space, with a step of 5° along the φ_2 axis for β -phase and along the φ_1 axis for α -phase, are presented.

Fig. 4. Geometry of the MGIXD method: constant α incident angle, $\psi_{\{hkl\}}$ angle between scattering vector and surface normal [19,20]. The sample coordinates TD , LD , and ND are indicated (during the tensile test, the load was applied along LD).

Fig. 5. Relative lattice strains $\langle \epsilon_{33}^{ph} \rangle_{\{hkl\}}$ vs sample strain E_{11} (Eq. 3) measured during the tensile test in the direction normal to the sample surface (ND). Experimental points are shown along with adjusted model functions (lines) for different hkl reflections (three Miller indices were used for reflections in hexagonal α phase). Model results obtained with SECs of β -phase from Ti-17 (a) and other sets of β -SECs given in Table 1 (b) are shown.

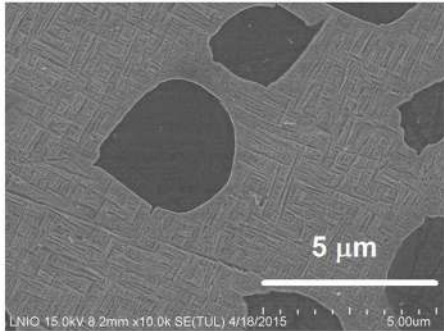
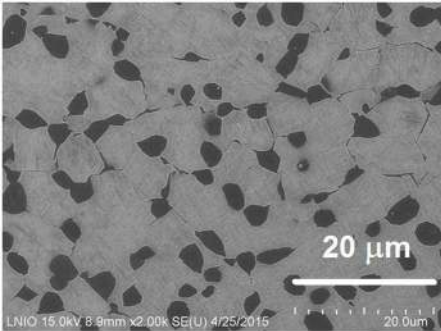
Fig. 6. Average lattice strains $\langle \epsilon_{33}^{ph} \rangle$ in the function of sample strain E_{11} in both phases. Experimental points are compared with model functions (lines).

Fig. 7. Mean accumulated shear strain (per one grain): for each slip system (a), for all systems and for the systems in each phase (b) as a function of the applied stress Σ_{11} .

Fig. 8. The $\langle a(\phi, \psi) \rangle_{\{hkl\}}$ vs $\sin^2 \psi$ plots determined for the initial sample without tensile loading for the applied load $\Sigma_{11}^{mech} = 1211$ MPa and for an unloaded sample after fracture. The experimental points and fitted lines are presented for α -phase (a) and β -phase (b).

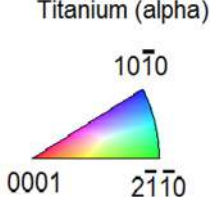
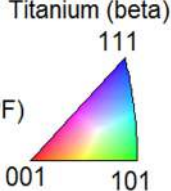
Fig. 9. Evolution of phase stresses σ_{11}^{ph} and σ_{22}^{ph} vs total sample strain E_{11} for α -phase (a) and β -phase (b), with thresholds corresponding to activation of slip systems (symbols are explained in Table 4). The stresses measured using MGIXD are compared with the model prediction for the parameters given in Table 4.

Fig. 10. Evolution of overall stresses Σ_{11} vs total sample strain E_{11} (a) and magnification of this plot for the elasto-plastic transition (b) determined from diffraction and loading cell and computed for the parameters given in Table 4. The thresholds corresponding to the activation of slip systems are shown.



Legend

Inverse Pole Figure (IPF)

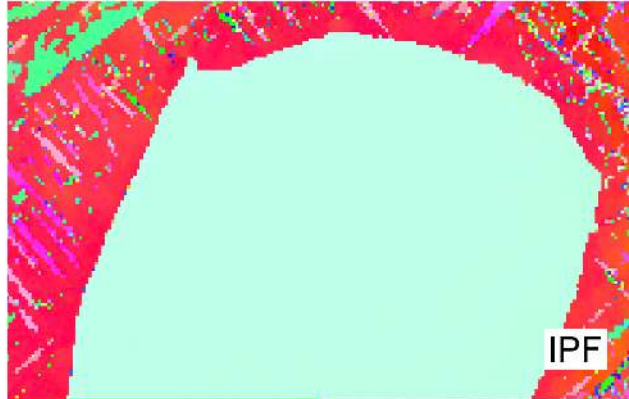
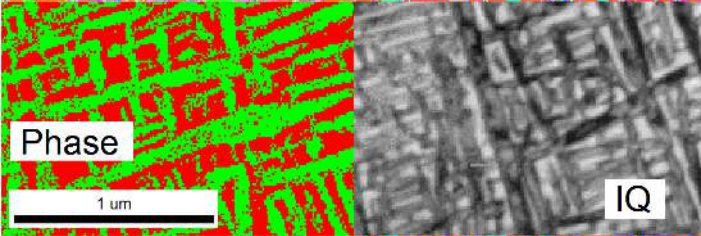
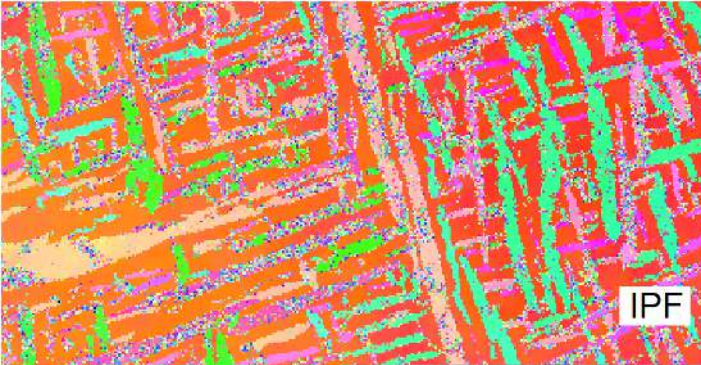


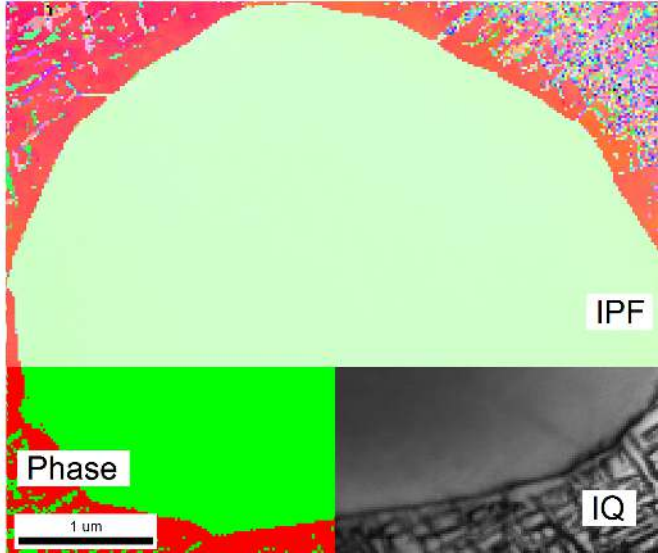
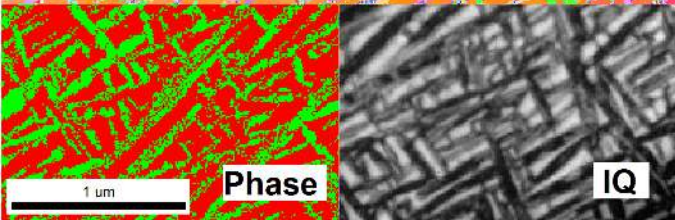
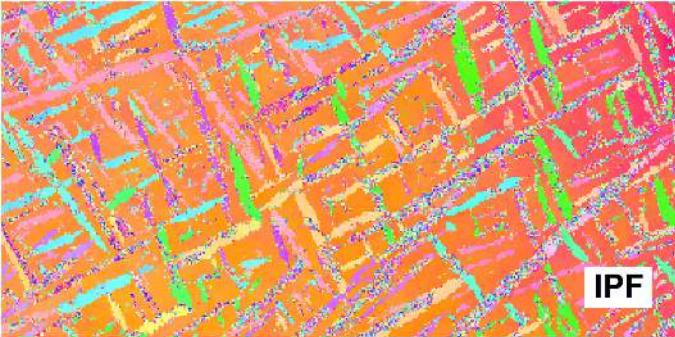
Phase Maps (Phase)



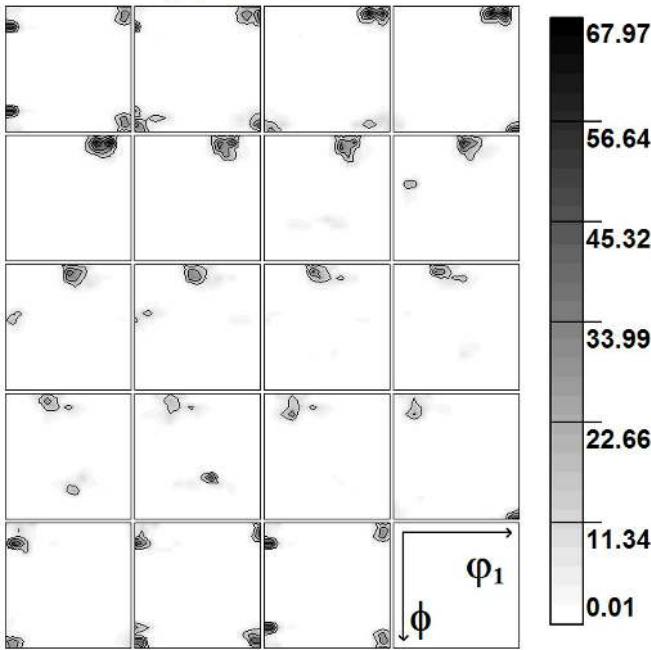
Image Quality (IQ)

gray scale maps: dark - low value
light - high value

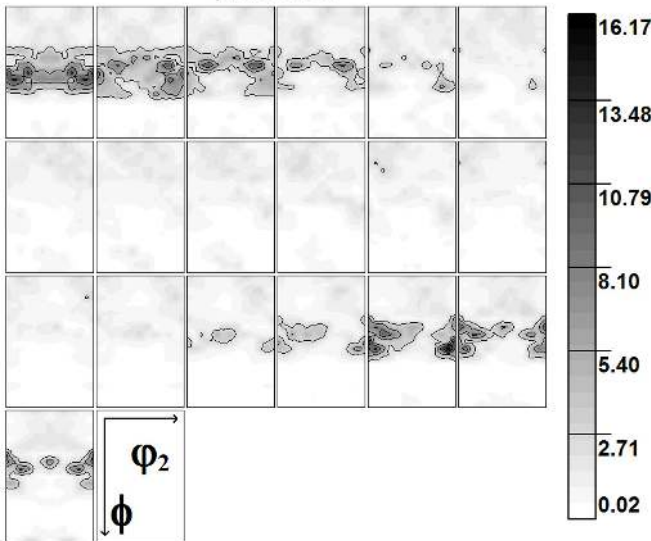


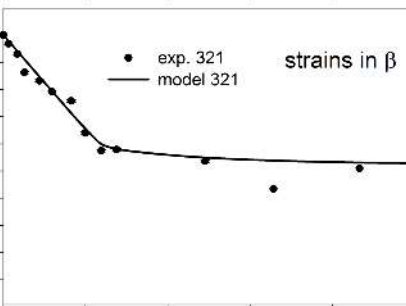
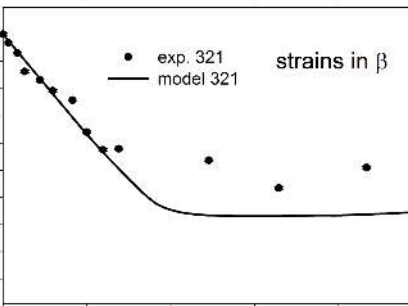
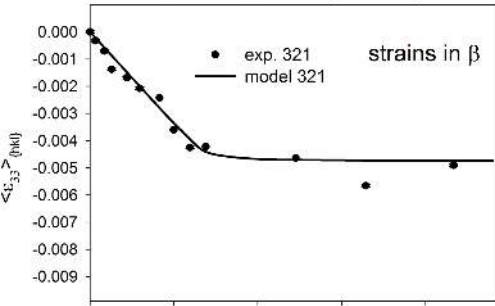
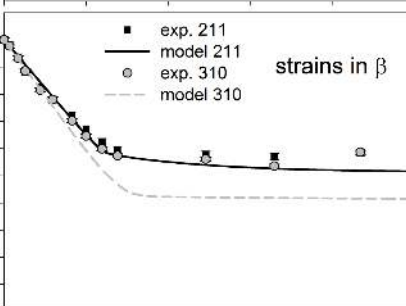
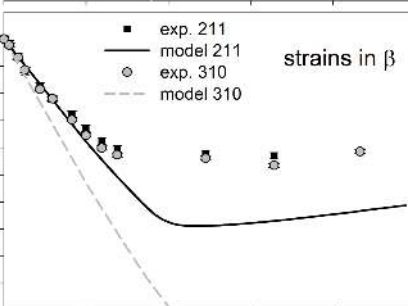
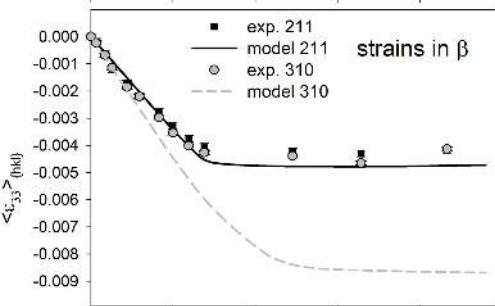
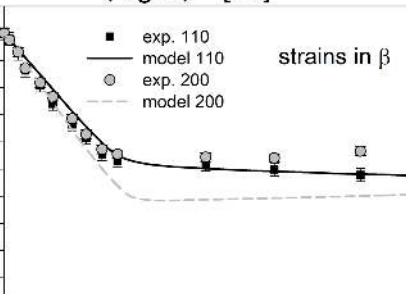
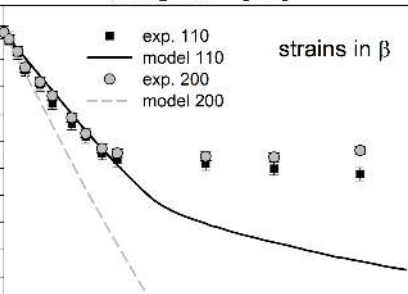
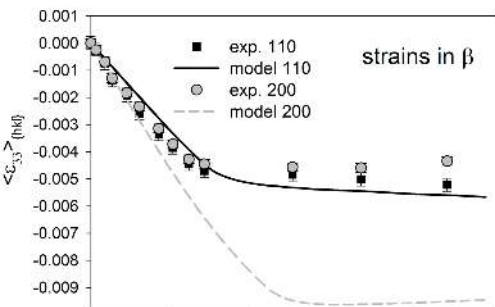


β -phase BCC

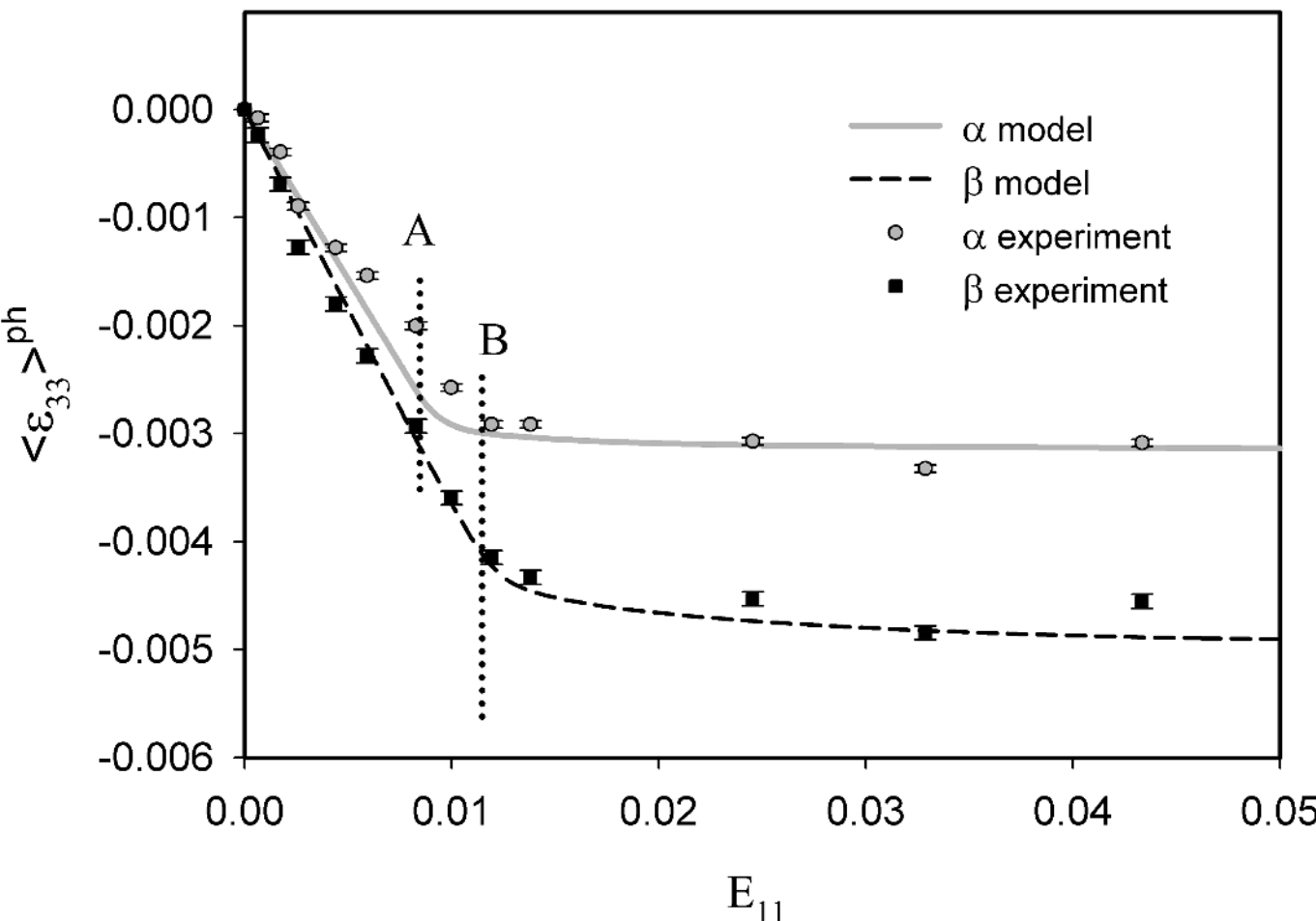


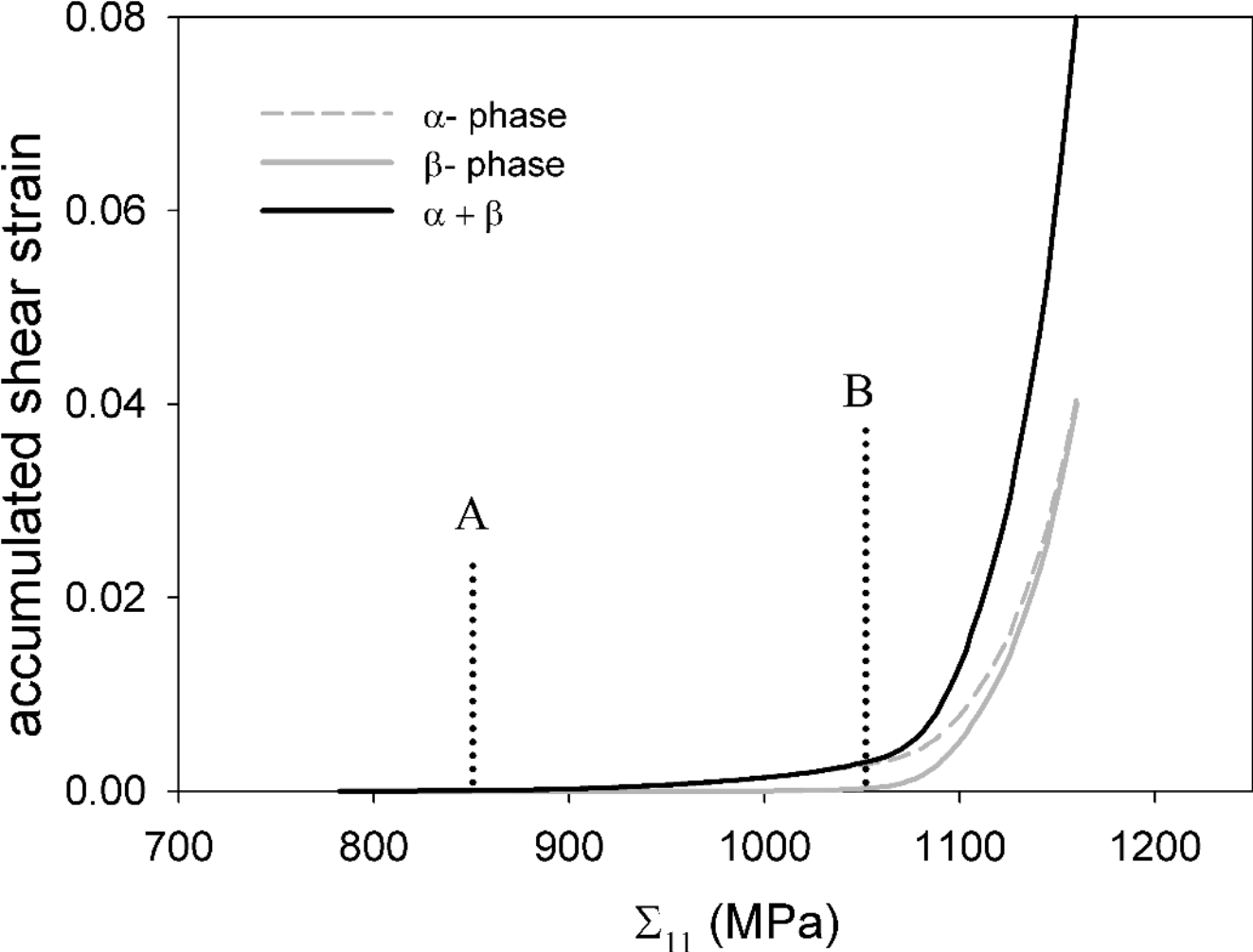
α - phase HCP



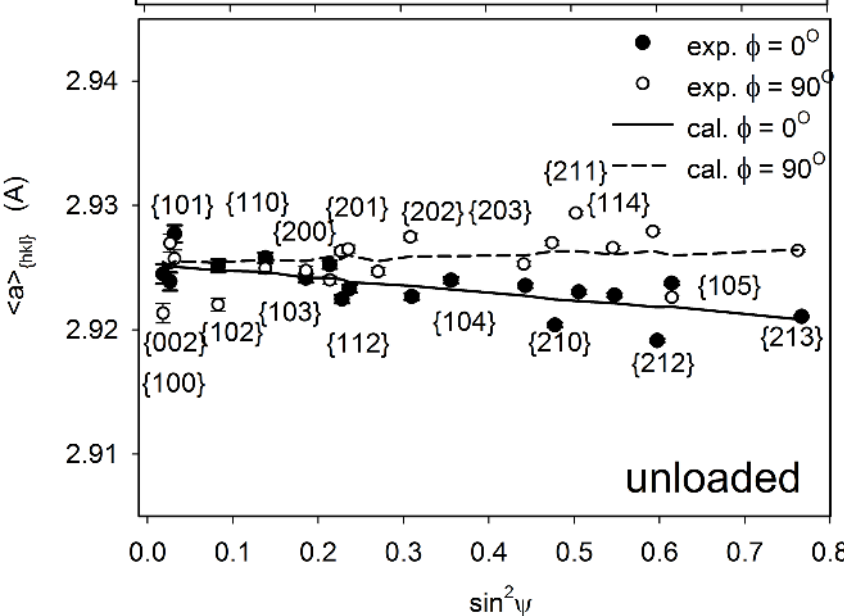
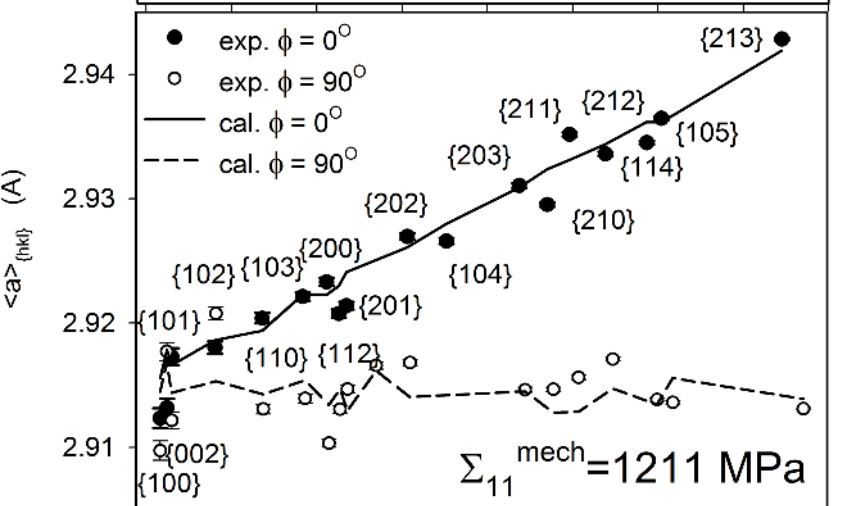
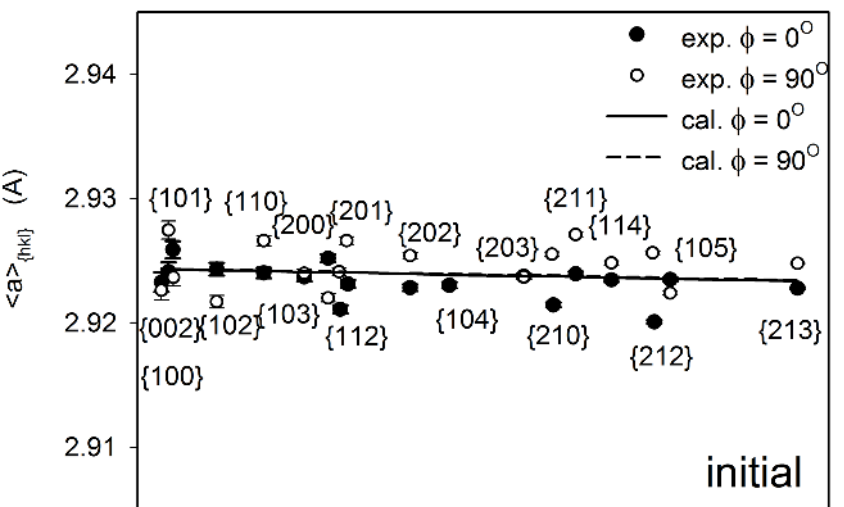
SECs of β from Ti-6Al-4V [15]SECs of β from Ti-10V-2Fe-3Al
(forged) [17]SECs of β from Ti-10V-2Fe-3Al
(aged) [17]

average strains

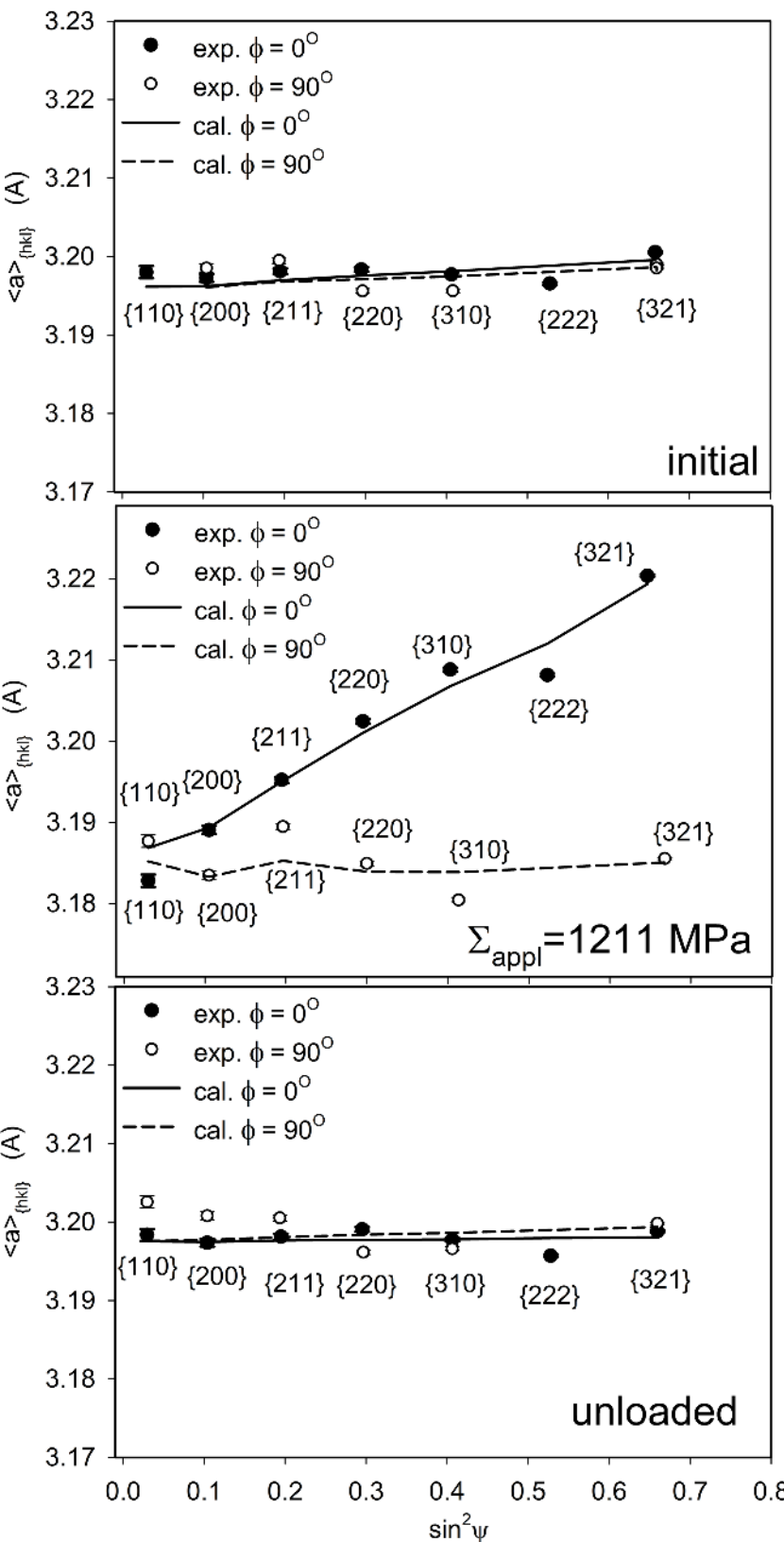


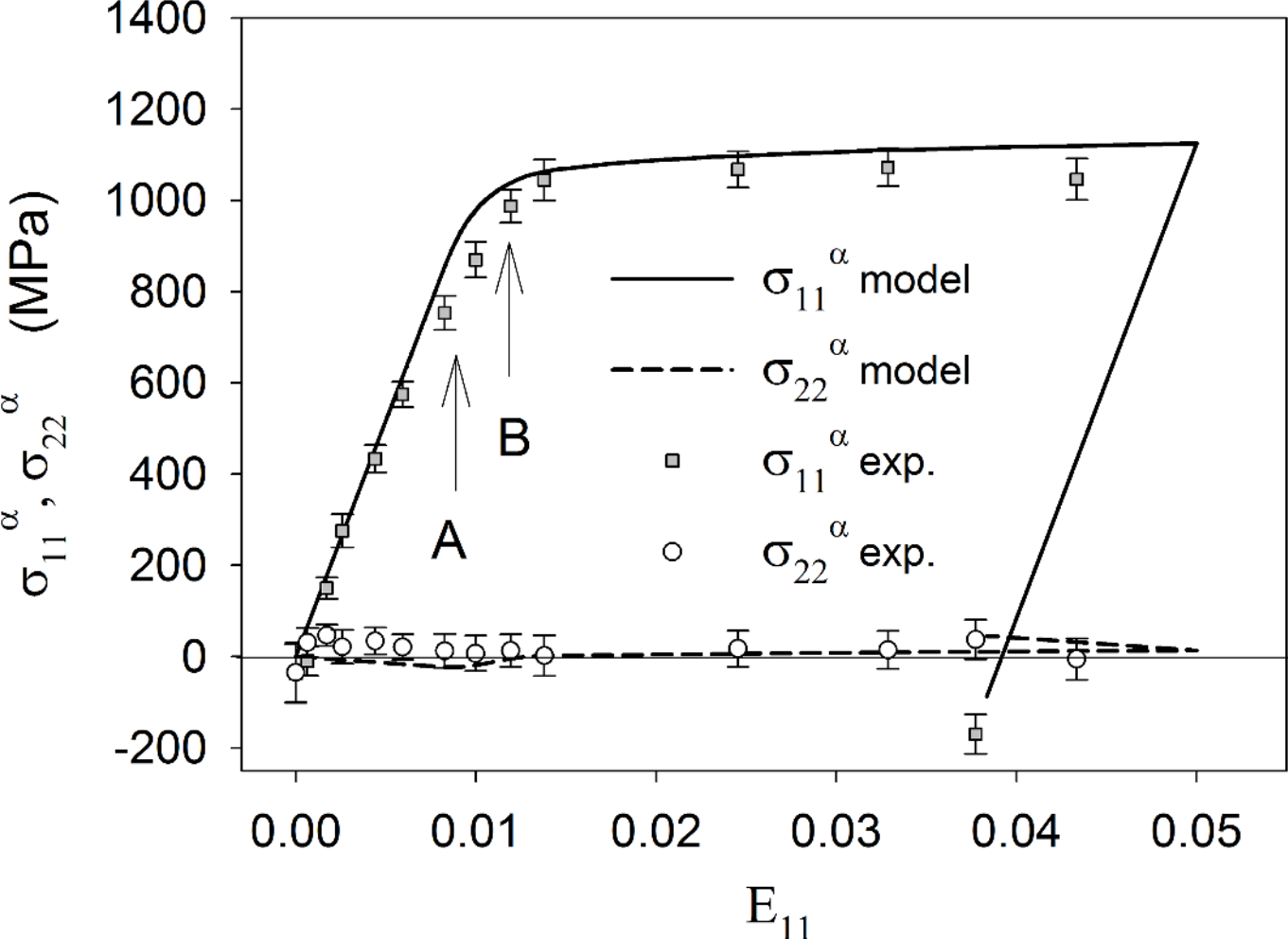


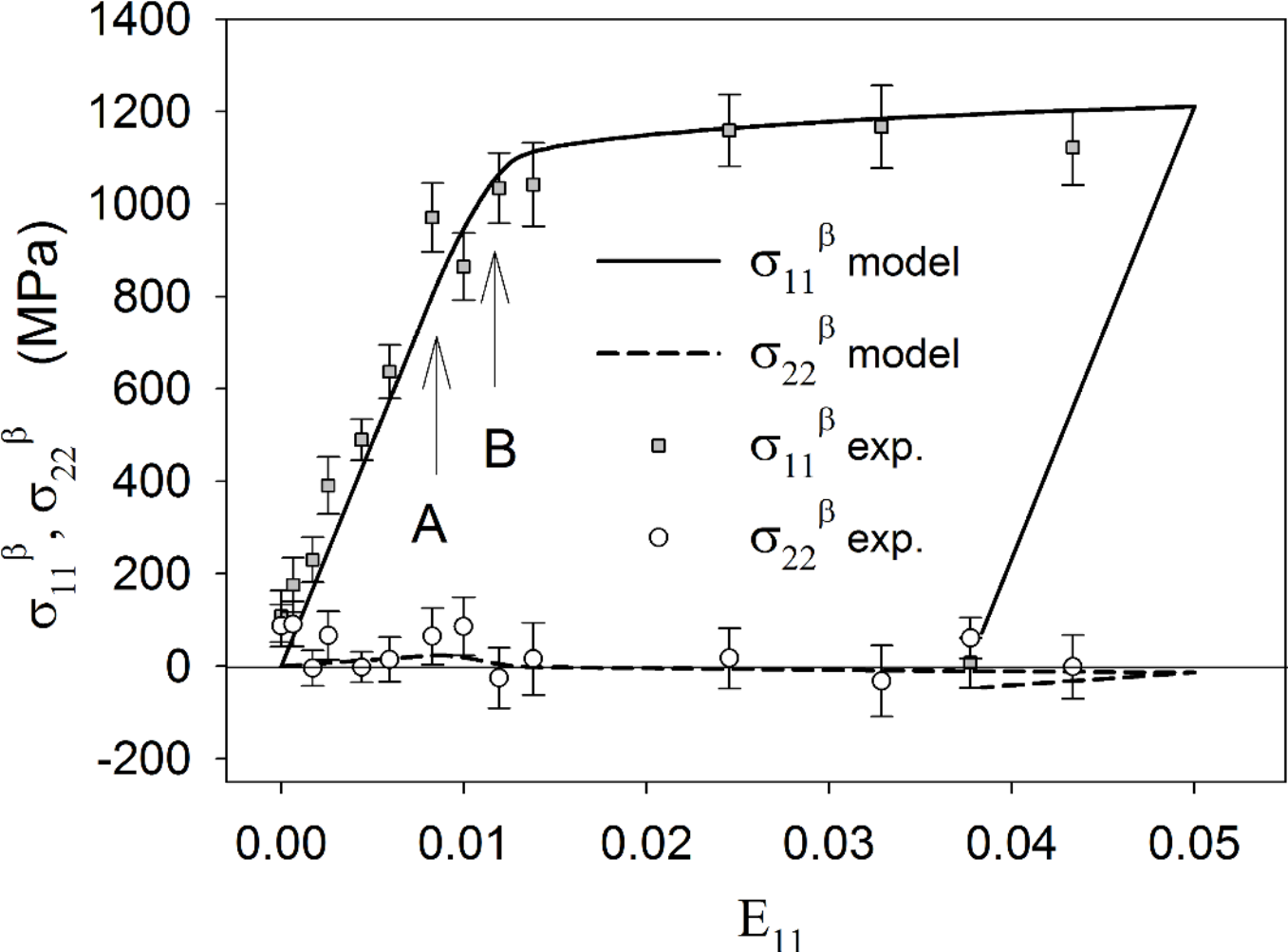
alfa

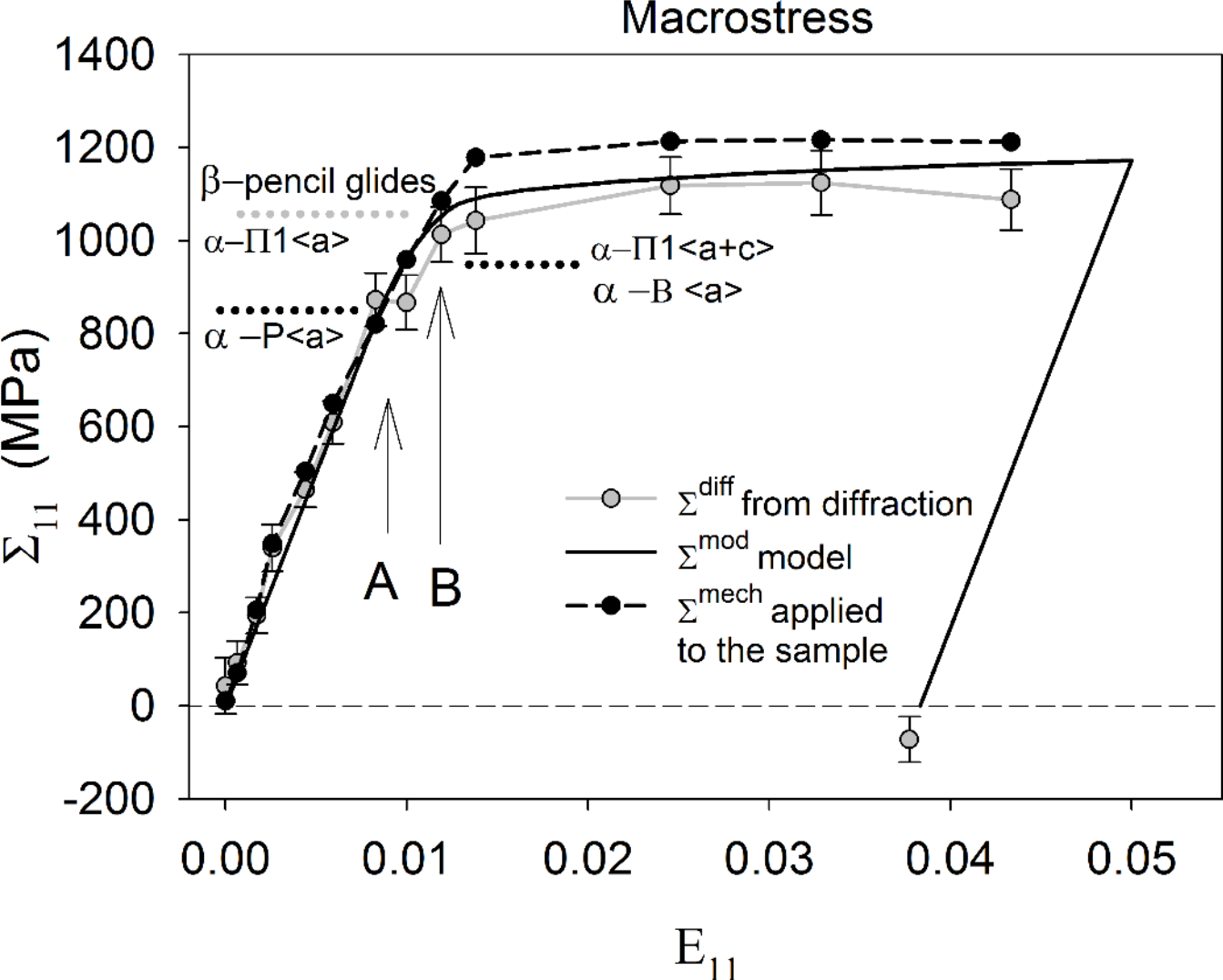


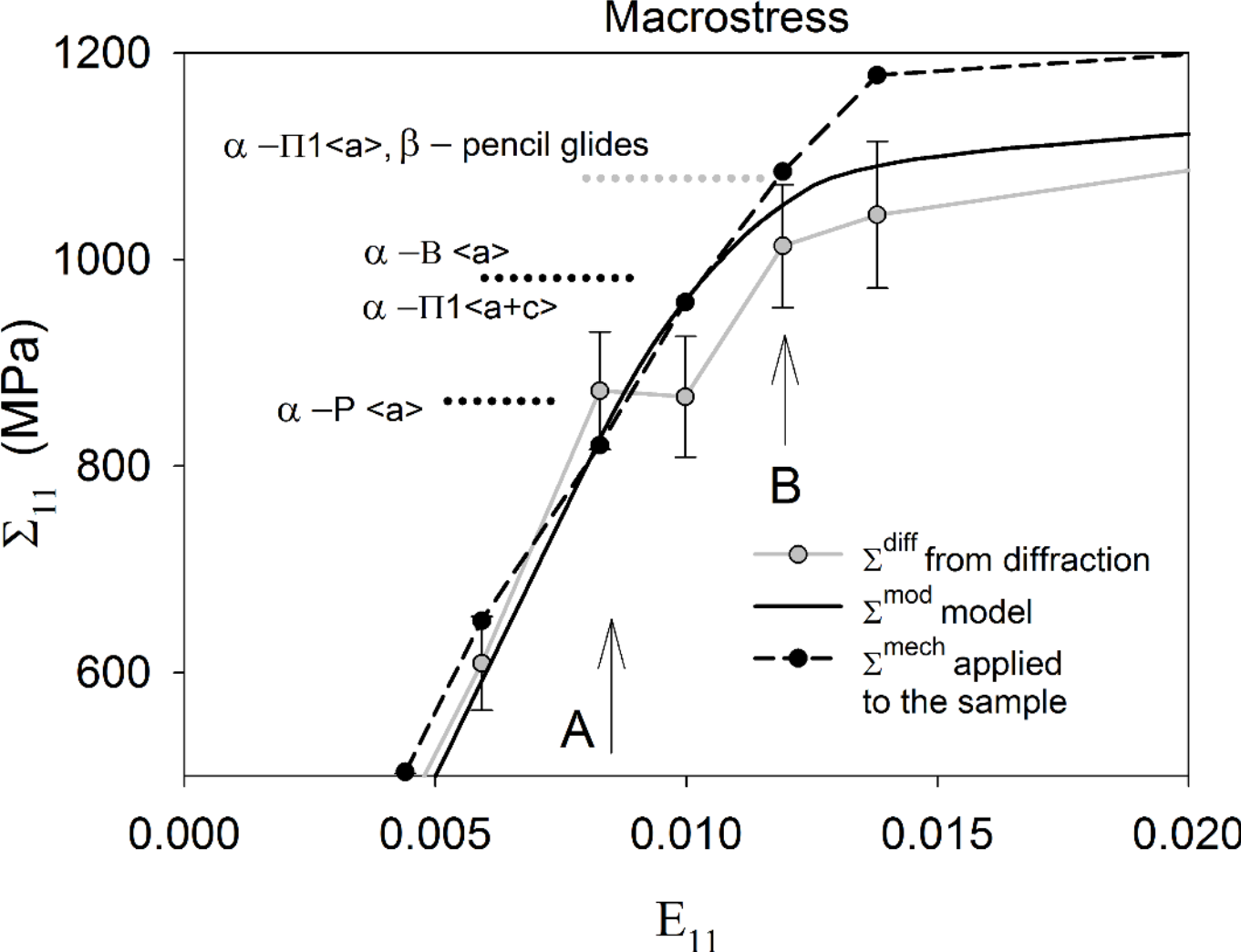
beta







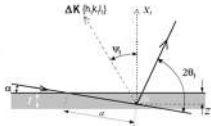




in situ
tensile
test

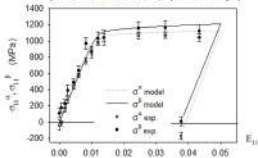


grazing
incidence
diffraction



two phase
Ti alloy

phase stresses (α and β)



slip activity

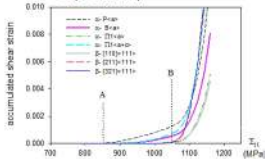


Table 1. Single crystal elastic constants (SEC) for α and β titanium, using the Voigt convention.

Phase	Material	c_{11} (GPa)	c_{12} (GPa)	c_{44} (GPa)	c_{13} (GPa)	c_{33} (GPa)	Zener factor A	Reference
α (hcp)	-	162	92	47	69	181	-	[19]
β (bcc)	Ti-17	174	116	41	$= c_{12}$	$= c_{11}$	1.4	[18]
	Ti-6Al-4V	138	108	51			3.4	[15]
	Ti-10V-2Fe-3Al (forged)	140	128	50			8.3	[17]
	Ti-10V-2Fe-3Al (forged and aged)	165	118	45			1.9	[17]

Table 2. The chemical composition in weight percentage of TIMETAL-18 (T-18) alloy.

Al	Mo	V	Cr	Fe	O	C	N	Ni	Ti
5.5	5.0	5.0	2.3	0.8	0.15	<0.1	<0.1	<0.1	Balance

Table 3. Symbols used for different types of stresses and strains.

Symbol	Meaning
E_{11}	Macroscopic strain of the sample (true strain), the same symbol used for experiment and model.
$\Sigma_{11}^{mech}, \Sigma_{11}^{mod}$	Macroscopic stress applied to the sample (true strain), symbol used for experiment and model, respectively.
σ_{ii}^{ph}	Phase stress determined using diffraction for ph – phase ($ph = \alpha$ or β).
Σ_{ii}^{diff}	Macroscopic stress determined from diffraction, i.e. the volume-weighted mean value $\Sigma_{ii}^{diff} = 0.45 \cdot \sigma_{ii}^{\alpha} + 0.55 \cdot \sigma_{ii}^{\beta}$.
$\langle \epsilon_{33} \rangle_{\{hkl\}}^{ph}$	Lattice strain measured using hkl reflection in ph - phase ($ph = \alpha$ or β).
$\langle \epsilon_{33} \rangle_{ph}$	Mean lattice strain calculated for ph - phase over all available reflections hkl ($ph = \alpha$ or β).

Table 4. Parameters of self-consistent model determined from tensile test.

Parameters of plasticity (MPa)	Phase	Slip system	Value (MPa)
τ_0^{ph}	α	Prismatic P $\{\bar{1}100\}\langle 11\bar{2}0 \rangle$	400
		Basal B <a> $\{0002\}\langle 11\bar{2}0 \rangle$	500
		Pyramidal $\Pi 1$ <a> $\{\bar{1}101\}\langle 11\bar{2}0 \rangle$	500
		Pyramidal $\Pi 1$ <c+a> $\{\bar{1}011\}\langle 11\bar{2}3 \rangle$	500
	β	Pencil glides: $\{011\}\langle 11\bar{1} \rangle$ $\{112\}\langle 11\bar{1} \rangle$ $\{123\}\langle 11\bar{1} \rangle$	520
H_0^{ph}	α	all systems	20
	β	all systems	20

Table 5. Values of phases stresses and macrostress determined from diffraction for Ti-18 alloy using different values of the SEC proposed in the literature. (the XSF were calculated accounting for texture using Kröner-Eshelby model). The last column shows the applied macrostress

Type of stress	Literature SECs of β -phase in specified materials				Σ^{mech} (MPa) applied stress
	Ti-17 [18]	Ti-6Al-4V [15]	Ti-10V-2Fe-3Al (forged) [17]	Ti-10V-2Fe-3Al (forged and aged) [17]	
σ^{α} (MPa) phase stress	1068 \pm 40				-
σ^{β} (MPa) phase stress	1169 \pm 77	876 \pm 40	549 \pm 26	1074 \pm 60	-
Σ^{diff} (MPa) macrostress	1113 \pm 62	948 \pm 53	768 \pm 37	1057 \pm 55	1211